

Covalent triazine reducing the defects by coordination roles and inhibiting I⁻ migration by anion-π interaction for efficient perovskite solar cell

Wenjing Hou^{a,*}, Mengna Guo^a, Tian Sun^b, Yaoming Xiao^c, Huan Bi^{d,*}, Yuxi Xu^{b,*}, Gaoyi Han^{a,*}

^a Institute of Molecular Science, Key Laboratory of Chemical Biology and Molecular Engineering of Education Ministry, Key Laboratory of Materials for Energy Conversion and Storage of Shanxi Province, Shanxi University, Taiyuan 030006, China

^b School of Engineering, Westlake University, Hangzhou 310024, China

^c College of Chemical Engineering and Materials Science, Quanzhou Normal University, Quanzhou 362000, China

^d Faculty of Informatics and Engineering, The University of Electro-Communications, Tokyo 182-8585, Japan



ARTICLE INFO

Keywords:

Covalent triazine frameworks (CTFs)

Anion-π interaction

Ion migration

Lead leakage

Perovskite solar cells

ABSTRACT

The grain boundary defects related non-radiative recombination, I⁻ migration, and lead leakage problems are the foundational and fundamental aspects for the perovskite solar cells. Herein, covalent triazine frameworks (CTFs) are introduced into the perovskite film to address these problems. CTFs can passivate the uncoordinated Pb²⁺ defects at grain boundary and reduce the lead leakage based on the coordination interaction between nitrogen atoms in triazine ring and Pb²⁺. CTFs can also inhibit the I⁻ migration and reduce the I⁻ vacancy defects based on the anion-π interaction between electron-deficient triazine ring and I⁻. Benefited from the passivated grain boundary defects and inhibited I⁻ migration by CTFs, the modified target device achieves a power conversion efficiency of 23.05 % with improved humidity stability and thermal stability. Therefore, this work lays the foundation for obtaining effective, stable, and environmentally friendly perovskite solar cells.

1. Introduction

Perovskite materials have attracted extensive attention in the photovoltaic field due to its easy solution processing and excellent semiconductor properties, such as high carrier mobility, low exciton binding energy and adjustable bandgap [1]. Because of above virtues, the organic-inorganic hybrid halide perovskite solar cell (PSC) has achieved a rapidly increased power conversion efficiency (PCE), holding the promise to become the next generation of prime photovoltaic techniques [2,3]. Nevertheless, some foundational and fundamental aspects should be considered for the perovskite solar cells, such as defects, recombination, or ion migration. The polycrystalline perovskite film will suffer the grain boundary defects due to the rapid crystallization process, especially for the iodine ion vacancy defects and uncoordinated Pb²⁺ defects [4]. The iodine ion (I⁻) in perovskite is liable to migrate along grain boundaries, and then leave I⁻ vacancy defects in its original position. The I⁻ migration can result in the unsatisfactory current and voltage hysteresis and halogen phase separation, especially for the wide-bandgap devices [5,6]. Furthermore, the I⁻ vacancy defects can accelerate the degradation of perovskite film by increasing the lattice

disorder. In addition, the uncoordinated Pb²⁺ is prone to dissolve and leakage due to its water-solubility, which pose a threat to the environment and human health [7]. Besides, the defects at grain boundary will act as a vulnerable spots for water and oxygen invading to accelerate the decomposition of perovskite film and lead leakage, especially in the aging conditions with high humidity and oxygen [8]. These defects can also cause undesired carrier non-radiative recombination and severe energy loss [9]. Therefore, it is essential to passivate the defects at grain boundary, reduce lead leakage, and inhibit the migration of I⁻ and the formation of I⁻ vacancy when promoting the application process of PSCs.

Chemical addition method has been widely employed to address above mentioned issues. Polymers, organic/inorganic salts, Lewis acid/base molecules, ionic liquids and nanoparticles have been employed to optimize the perovskite absorption layer and reduce defects [10,11]. These additional materials play multiple roles, such as adjusting the morphology of the perovskite film, interacting with uncoordinated ions to inhibit ion migration, adjusting the material level alignment, eliminating hysteresis, and improving device stability [12-14]. Except for above materials, the frame materials have also been widely used in the

* Corresponding authors.

E-mail addresses: houwenjing@sxu.edu.cn (W. Hou), hbi.trans.sci@gmail.com (H. Bi), xuyuxi@westlake.edu.cn (Y. Xu), han_gaoyi@sxu.edu.cn (G. Han).

photovoltaic field because of its high specific surface area, excellent stability and regular pore structure. For example, Tang et al. have used the PbX_2 ($X = \text{Cl}, \text{Br}$) to catalyze the 4,4',4''-(1,3,5-triazine-2,4,6-triphenyl) triphenylamine (BPT) and 4,4'- biphenyldicarboxaldehyde (BPDA) to form the two-dimensional conjugated covalent organic framework (COFs) on the surface and grain boundary in situ, which has passivated harmful defects at the grain boundary, reduced non-radiative recombination and inhibited halide segregation in mixed halide perovskite by inhibiting I^- migration at the grain boundary [15]. Liu et al. found that adding donor-acceptor COF materials to the perovskite layer can reduce defect density and improve charge separation efficiency [16]. In addition, Seok et al. synthesized COF materials through monomer reaction to inhibit perovskite degradation and formation of undesirable perovskite phases. Moreover, the strong conjugation and π - π interaction of COF materials make perovskite crystallize well [17]. Yang et al have employed the as-synthesized indium-based metal-organic

framework (MOFs) nanocrystals to regulate the perovskite crystallization and passivate the surface and grain boundary defects, so as to obtain high-quality perovskite film and improve device performances [18]. In addition, Wu et al. have utilized MOF material to capture Pb^{2+} in solution by forming an insoluble solid, thereby reducing environmental pollution [19].

As one type of novel COF materials, covalent triazine frameworks (CTFs) material formed by connected triazine ring and benzene ring is a kind of porous material with good thermal and chemical stability. This kind of material has great application prospects in the fields of gas adsorption and separation, energy storage and conversion, and heterogeneous catalysis due to its full cyclic conjugated structure, aromatic nitrogen rich skeleton, high Brunauer-Emmet-Teller (BET) surface area and precise porosity, etc [20,21]. The nitrogen atom in the covalent triazine ring has the function of Lewis base due to its lone electron pairs. Although the triazine ring is aromatic and nitrogen-rich, the previous

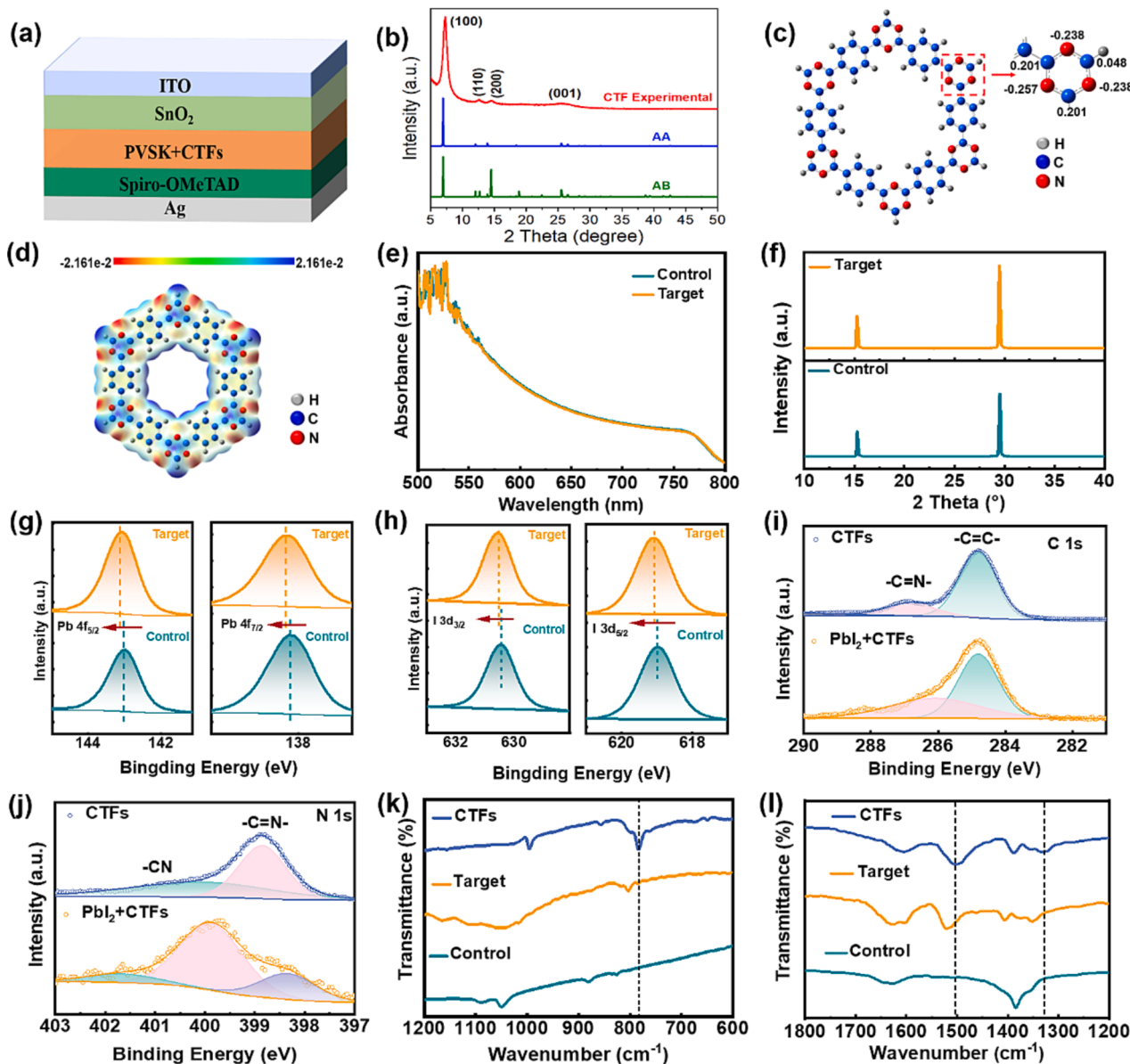


Fig. 1. (a) Device architectures with CTFs modification; (b) Experimental (red), simulated AA stacking (blue) and AB stacking (green) PXRD patterns of CTFs; (c) Milliken charge distribution and (d) calculated electrostatic potential (ESP) profile of the CTFs; (e) UV-Vis absorption spectra and (f) XRD patterns of the perovskite films; Locally magnified Pb 4f and I 3d XPS spectra of perovskite films without and with CTFs; (g) Pb $4\text{f}_{5/2}$ and Pb $4\text{f}_{7/2}$ peaks for Pb 4f, and (h) I $3\text{d}_{3/2}$ and I $3\text{d}_{5/2}$ peaks for I 3d; (i) C 1s and (j) N 1s XPS spectra of CTFs before and after being introduced into PbI_2 ; FTIR spectra of the CTFs and perovskite film without and with CTFs modification in different wavenumber range: (k) in $600\text{--}1200\text{ cm}^{-1}$ and (l) in $1200\text{--}1800\text{ cm}^{-1}$.

reports have mentioned that the whole triazine ring is electron-deficient owing to the fact that the lone pair electrons on the hybrid type of N atom cannot participate in the conjugation of triazine ring [22].

In this paper, CTFs material has been introduced into perovskite precursor solution for device fabrication. The nitrogen atom on the triazine ring in CTFs has the function of Lewis base because of its lone electron pair, so it can passivate the uncoordinated Pb^{2+} defect at the grain boundary of perovskite. Besides, the triazine ring is electron-deficient, because the lone pair electrons on the hybrid N atom cannot participate in the conjugation of the triazine ring. The electron-deficient triazine ring can form anion- π interaction by getting electrons from I^- , which is conducive to inhibit undesired I^- migration. In addition, CTFs can also be used to adsorb Pb^{2+} and reduce the lead leakage based on the framework structure of CTFs and chemical bond between CTFs and Pb^{2+} . As a result, the CTFs-modified device yields a PCE of 23.05 %, higher than that of the control device (21.26 %). The CTFs-modified device presents enhanced moisture and thermal stability and the effect for suppressing lead leakage.

2. Results and discussion

As the Fig. S1 shown, the CTFs were prepared according to the previous reports [20]. The as-prepared CTFs were introduced into the perovskite precursor solution to study the effects on device performances. As shown in Fig. 1a, our work is based on the device structure of ITO/SnO₂/perovskite (CTFs)/Spiro-OMeTAD/Ag, where the component of perovskite was $\text{Rb}_{0.02}(\text{FA}_{0.95}\text{Cs}_{0.05})_{0.98}\text{Pb}(\text{I}_{0.97}\text{Br}_{0.01}\text{Cl}_{0.02})_3$. In Fig. 1b, the powder X-ray diffraction (PXRD) peak at 7.24°, 12.40°, 14.53° and 25.70° are assigned to the diffraction of (100), (110), (200) and (001) crystal plane of CTFs. The previous study has indicated the CTFs mostly present eclipsed AA-stacking model and staggered AB-stacking model [23]. By comparing the experimental PXRD of CTFs with eclipsed AA-stacking and staggered AB-stacking models, it is found that the obtained CTFs showed the typical feature of AA-stacking model. This also proves that covalent triazine with pure phase was synthesized successfully. CTFs are a class of porous framework materials composed of triazine rings and benzene rings. As the transmission electron microscope (TEM) and corresponding mapping proved in Fig. S2, CTFs can be exfoliated into two-dimensional nanosheets containing N and C atoms. And the AFM characterization in Fig. S3 presents that the average thickness of CTFs nanosheet is about 1.5 nm. The N_2 adsorption results in Fig. S4 illustrate that CTFs possess the BET specific surface area of 1494.75 m² g⁻¹. Besides, CTFs have porous structure with the main pore size of 1.1 nm, which provides a spatial advantage for the subsequent lead adsorption. The Milliken charge distribution (Fig. 1c) illustrates that the N atoms in triazine ring exhibit the negative charge, while the C atoms in triazine ring show the positive charge. The electrostatic potential (ESP) shown in Fig. 1d proves the N atoms in triazine ring possess the higher electron density than the C atoms region, which can be attributed to the N atom has the lone pair electrons. The triazine ring provides favorable conditions for passivating the uncoordinated Pb^{2+} by donating the electrons from N atoms in triazine ring. In addition, the electron-deficient triazine ring in CTFs can attract the electrons from I^- anion by forming classical anion- π interaction [24–26]. As the Fig. 1e and Fig. 1f shown, the unchanged UV-vis adsorption peak intensity and XRD peak location indicate that CTFs have little influence on the absorption properties and composition of perovskite films. The Tauc diagram in Fig. S5 reveals that CTFs will not change the band gap (E_g) of perovskite film (1.53 eV). Besides, the unchanged XRD peak position also indicate the CTFs can not enter the lattice to interfere with the 3D frame structure of perovskites. After introducing the CTFs, the increased XRD diffraction intensity indicates that CTFs can enhance the crystalline properties of perovskite film, which can be deduced from the possible chemical interaction between CTFs and precursor composition. In order to prove this opinion, the Locally magnified XPS spectra of perovskite (PVSK) and CTFs + PVSK were presented in Fig. 1g-h. It can be seen that

after CTFs modification, the XPS peaks of $\text{Pb } 4\text{f}_{5/2}$ at 142.97 eV and the $\text{Pb } 4\text{f}_{7/2}$ at 138.17 eV move to the higher binding energy direction. Besides, the XPS peaks of $\text{I } 3\text{d}_{3/2}$ (630.47 eV) and $\text{I } 3\text{d}_{5/2}$ (618.97 eV) also shift to the higher binding energy direction. I^- can interact with triazine ring by donating its electrons to electron-deficient triazine ring. The decreased electron density on I^- results in the higher-shifted binding energy. The changed binding energy of $\text{Pb } 4\text{f}$ and $\text{I } 3\text{d}$ can illustrate that the CTFs can exert the chemical interaction with perovskite. The XPS spectra of C 1s and N 1s are tested to prove the possible chemical interaction between CTFs and Pb/I atoms. As the Fig. 1i shown, the XPS peaks of C 1s with a binding energy of 286.75 eV and 284.80 eV are assigned to the characteristic peaks of $-\text{C}=\text{N}-$ for triazine ring and $-\text{C}=\text{C}-$ for benzene ring, respectively. After introducing into PbI_2 , the binding energy of $-\text{C}=\text{C}-$ has no obvious shift, while the binding energy of $-\text{C}=\text{N}-$ shift to the lower value, indicating the $-\text{C}=\text{N}-$ bond in triazine ring is the main action site. In Fig. 1j, the XPS peaks of N 1s in C-N (400.15 eV) and C=N (398.90 eV) shifted to the higher binding values, which can be attributed to the fact that CTFs can donate the lone pair electrons of N atoms. In addition, the newly generated peak at 398.37 eV can be attributed to the formation of N-Pb bond between the triazine ring and the uncoordinated Pb^{2+} . Above results all illustrate that the CTFs can exert strong chemical interaction with perovskite. In order to characterize the interaction between CTFs and perovskite films further, we test the fourier transform infrared spectroscopy (FTIR). The vibration peaks at 784.29 cm⁻¹, 1332.05 cm⁻¹ and 1503.71 cm⁻¹ are belong to the vibration peaks of triazine ring [20], and the latter two are belong to the stretching vibration peaks of -C-N and -C=N in CTFs. After introducing CTFs into perovskite films, the above three peaks all shift to the higher wavenumber, indicating the chemical interaction exists between CTFs and perovskite.

The density functional theory (DFT) calculations have been conducted to interpret the possible interaction between CTFs and perovskite. Fig. S6 depicts the optimized configurations of CTFs-modified perovskite with different terminal surfaces. In Fig. 2a-d, the charge difference is calculated to evaluate the interaction between CTFs and perovskite with different surface, including the perfect Pb-I surface, Pb-I surface with V_1 , perfect FA-I surface, and FA-I surface with V_1 . Yellow and blue colors represent the regions gained and lost electrons. In Fig. 2a-d, the obvious electron transfer can be observed between CTFs and perovskite surface regardless of the presence or absence of V_1 . For the Pb-I terminated surface in Fig. 2a-b, the blue triazine ring and yellow Pb^{2+} indicate that the CTFs can passivate the uncoordinated Pb^{2+} defects by donating the electrons of N atoms to Pb^{2+} . And for the FA-I surface in Fig. 2c-d, the electrons from I^- can transfer to triazine ring in CTFs, because the electron-deficient triazine ring can attract negative charge on I^- and form anion- π interaction. The charge differences at the 2D slice of (010) plane of perovskite are employed to study the electron transfer between CTFs and perovskite with different surface in Fig. 2e-h. It is obvious that CTFs can significantly interact with perovskite regardless of the exposed surface. Fig. 2i-l is the drawing about differential charge densities vs. the position in the Z direction [27]. In Fig. 2i-j, CTFs exhibit the strong electron interaction with the Pb-I terminal perovskite surface, because CTFs can coordinate with the uncoordinated Pb^{2+} defects. Especially, the electron interaction between CTFs and FA-I surface with V_1 defects is the strongest, indicating the evident interaction exists between CTFs and I^- .

A molecular simulation method has also been adopted to study the detailed interaction between CTFs and I^- . And the independent gradient model based on Hirshfeld partition (IGMH) is utilized to present the gradient of electron density across the CTFs and I^- , because IGMH performs significantly well in studying and revealing the weak interactions [28]. As the $\text{sign}(\lambda_2)\rho$ colored method shown in Fig. 3a and b, the isosurface with different colors represent the different types of interactions. To be more specific, red, green and blue isosurface stand for the repulsive interaction, van der Waals interaction, and weak interaction (H-bond or halogen-bond), respectively (Fig. S7) [29]. And for the

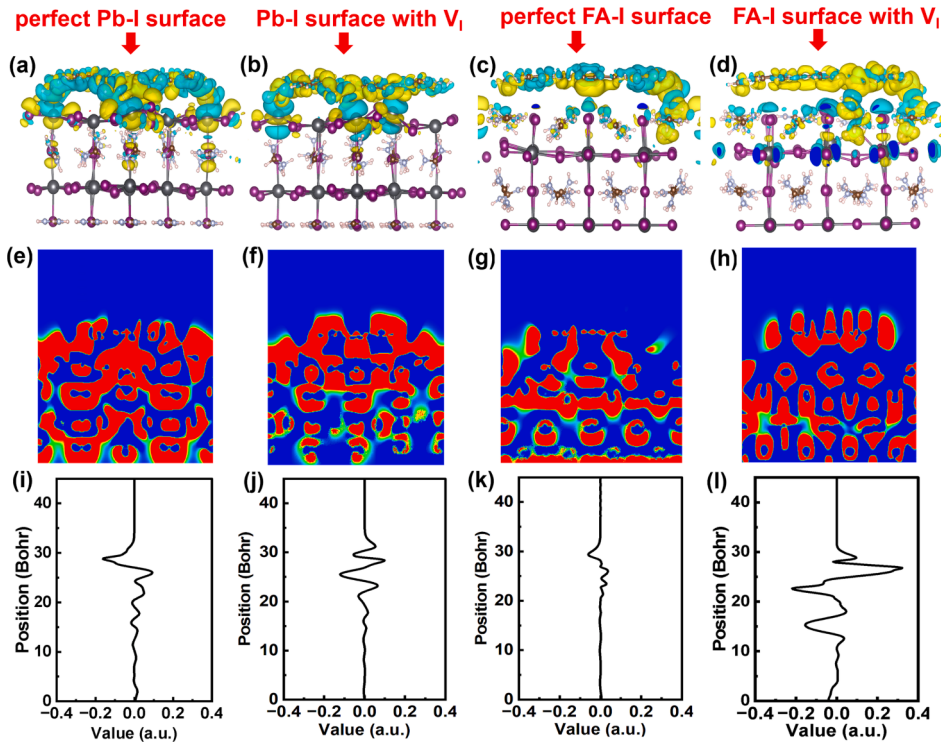


Fig. 2. Interaction study between CTFs and perovskite with different surface: (a, e, i) perfect Pb-I surface, (b, f, j) Pb-I surface with V_I , (c, g, k) perfect FA-I surface, and (d, h, l) FA-I surface with V_I . (a-d) 3D Charge difference between CTFs and perovskite, (e-h) Charge difference at the 2D slice of (010) plane of perovskite; (i-l) Differential charge densities at CTFs/perovskite surface. The longitudinal axis represents the position in the Z direction.

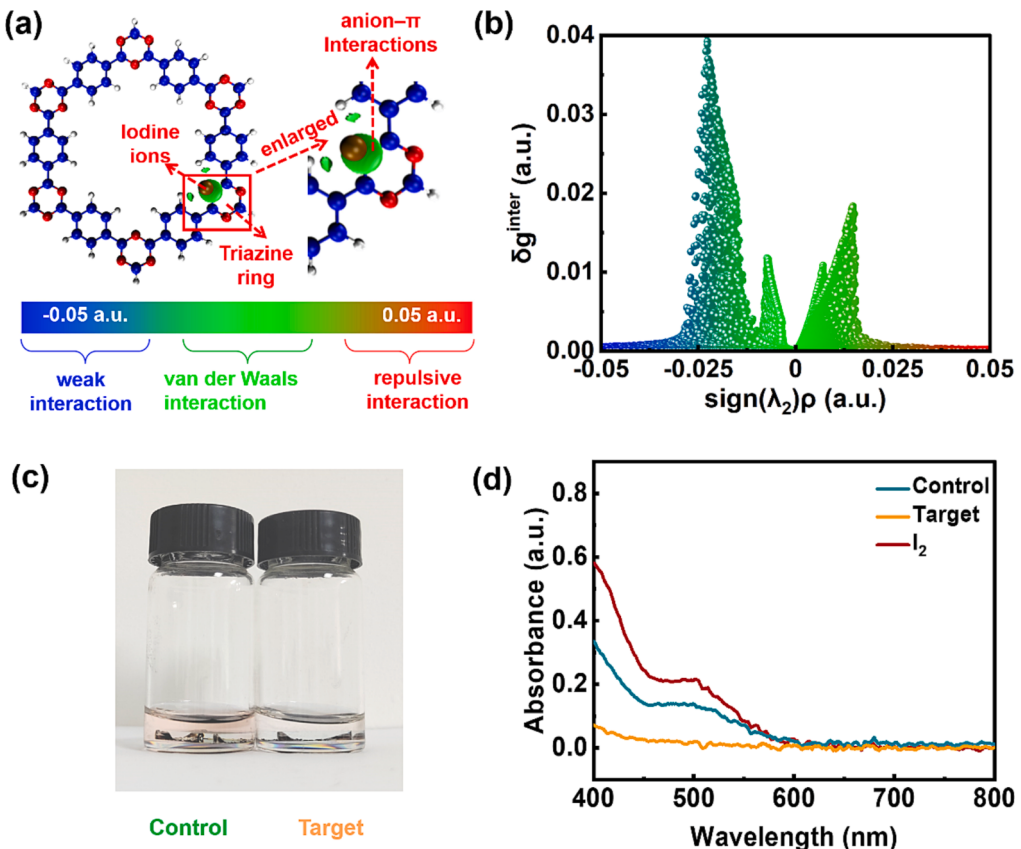


Fig. 3. (a) $\text{sign}(\lambda_2)\rho$ colored IGMH map for CTFs and I^- with isovalue (δg) of 0.005 a.u.; (b) Scatter graph of IGMH for revealing the interaction between CTFs and I^- ; (c) A photo of control and target perovskite films soaked in a sealed vial filled with toluene solution under 1-sun illumination for 8 h; (d) Ultraviolet absorption spectra of toluene leaching solution of iodine and control and target perovskite films.

IGMH map, the isosurface between triazine ring of CTFs and I^- mainly exhibits green color, indicating the interaction between CTFs and I^- is van der Waals. In fact, anion- π interaction is one of a typical van der Waals interaction.

CTFs is expected to inhibit I^- migration due to the interaction between triazine ring and I^- . The dissociative I^- in device tends to migrate, combine, and be oxidized to form I_2 , which is unfavorable to the device performances [30]. I_2 release has been used to characterize the I^- migration indirectly by conducting the toluene soaking experiment in previous reports by Henry J. Snaith and Huang et al. Toluene is selected as an effective solvent because of its non-destructive to perovskites [30–32]. In addition, toluene can be used as an effective solvent to determine the iodine content by UV–Vis absorption spectrum [33]. After being exposed to 1-sun illumination for 8 h, the toluene leaching solutions of control and target perovskite films are used to test the ultraviolet absorption spectra for proving the inhibition effect of CTFs on I_2 release caused by I^- migration. In Fig. 3c and d, the toluene leaching solution of control perovskite film presents pink color, which presents a significant I_2 absorption peak at 500 nm [30]. On the contrast, the toluene leaching solution of target film is still colorless and does not appear adsorption peak at 500 nm, which proves the suppressed I_2 release by CTFs. Above results indirectly indicate that the CTFs modification can inhibit the I^- migration. The anion- π interaction between CTFs and I^- can fixes I^- and prevent it from migrating and combining to form I_2 .

We have analyzed the effect of CTFs additive on the morphology of perovskite films by observing SEM images. Fig. 4a-b and Fig. S8–S9 show that CTFs modification has influenced the grain size of perovskite film. When the CTFs concentration increases from 0 mg/mL to 0.20 mg/mL, the grain size of perovskite films increases from 1.35 μ m to 1.44 μ m. However, when the concentration increases from 0.20 mg/mL to 0.23

mg/mL, the grain size decreases, which means the increased grain boundary number. As shown in Fig. 4c and d, the control and target perovskite films show the cross-sectional thickness about 500 nm. As shown in Fig. 4e–j, C-AFM tests have been performed on control and target perovskite films. The corresponding test results are based on a line through the grain and boundaries in the pictures. And the number 1, 2, 3 and 4 on line denote different grain boundaries (GBGs). In Fig. 4e and h, the root mean square (RMS) value decreases from 23.50 nm of the control film to 17.20 nm of the CTFs-modified film, indicating that the surface of the perovskite film is smoother after CTFs modification. Therefore, CTFs modification is helpful to improve the morphology of perovskite films. The Fig. 4f and i present the tunneling current distribution mapping at grains and their boundaries. The previous reports have revealed that the defects at grain boundaries are responsible for the increased electrical conductivity and ion migration, which decides that the current at grain boundary is higher than that in grain interiors. And the higher current at grain boundary represents the high trap density [34,35]. In Fig. 4g and j, the changes of curves for height and dark current are corresponding to the straight lines. The dark current at the grain boundary of the target film is dramatically reduced, indicating the effectively passivated defects and reduced carrier recombination at grain boundary. This results indirectly illustrate the CTFs are located at the grain boundaries of perovskite.

For the space-charge-limited-current (SCLC) model in Fig. 5a, the defect density (n_t) of perovskite films can be estimated quantitatively according to the equation (1) [36]:

$$n_t = \frac{2\epsilon\epsilon_0 V_{TFL}}{eL^2} \quad (1)$$

where ϵ is the relative dielectric constant of perovskite, ϵ_0 the

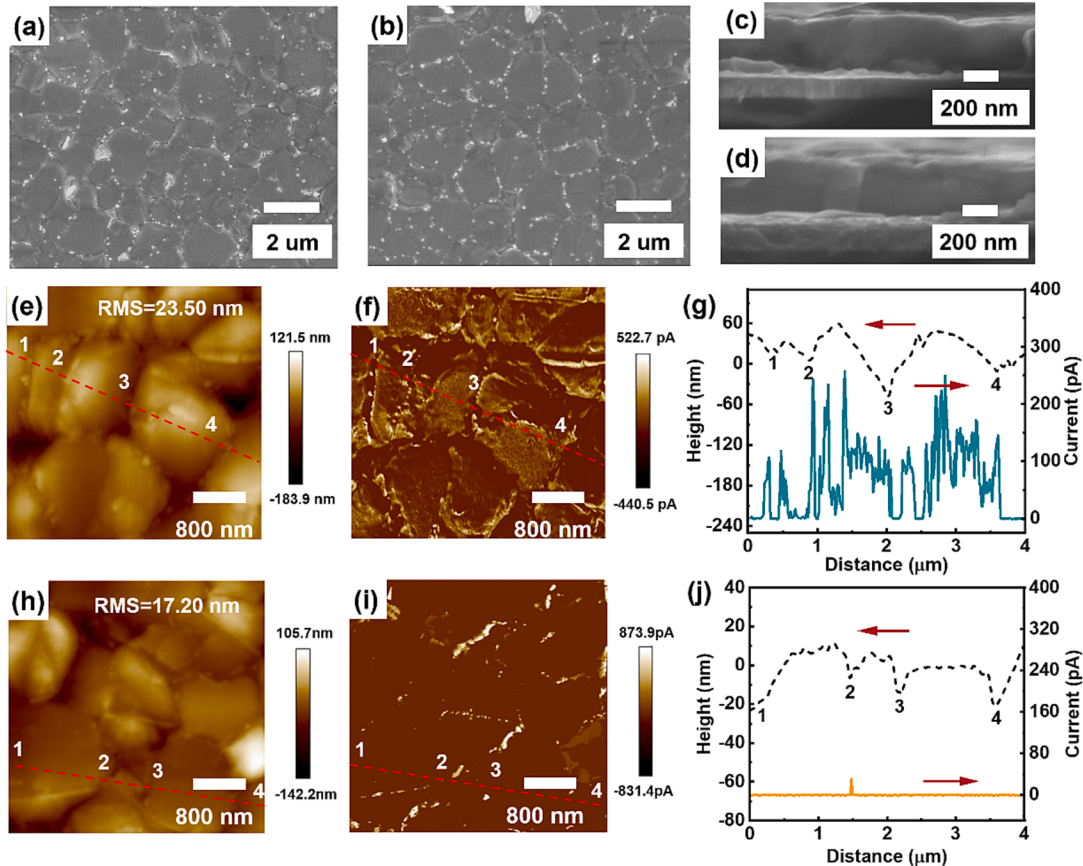


Fig. 4. Top-view and cross-sectional scanning electron microscope (SEM) images of: (a and c) control perovskite films and (b and d) target perovskite films; Conductive atomic force microscopy (C-AFM) of perovskite films with different presentation modes: (e and h) height mapping images; (f and i) current mapping images and (g and j) Height/current along scan distance. The results are assigned to (e–g) control film and (h–j) CTFs-modified target film.

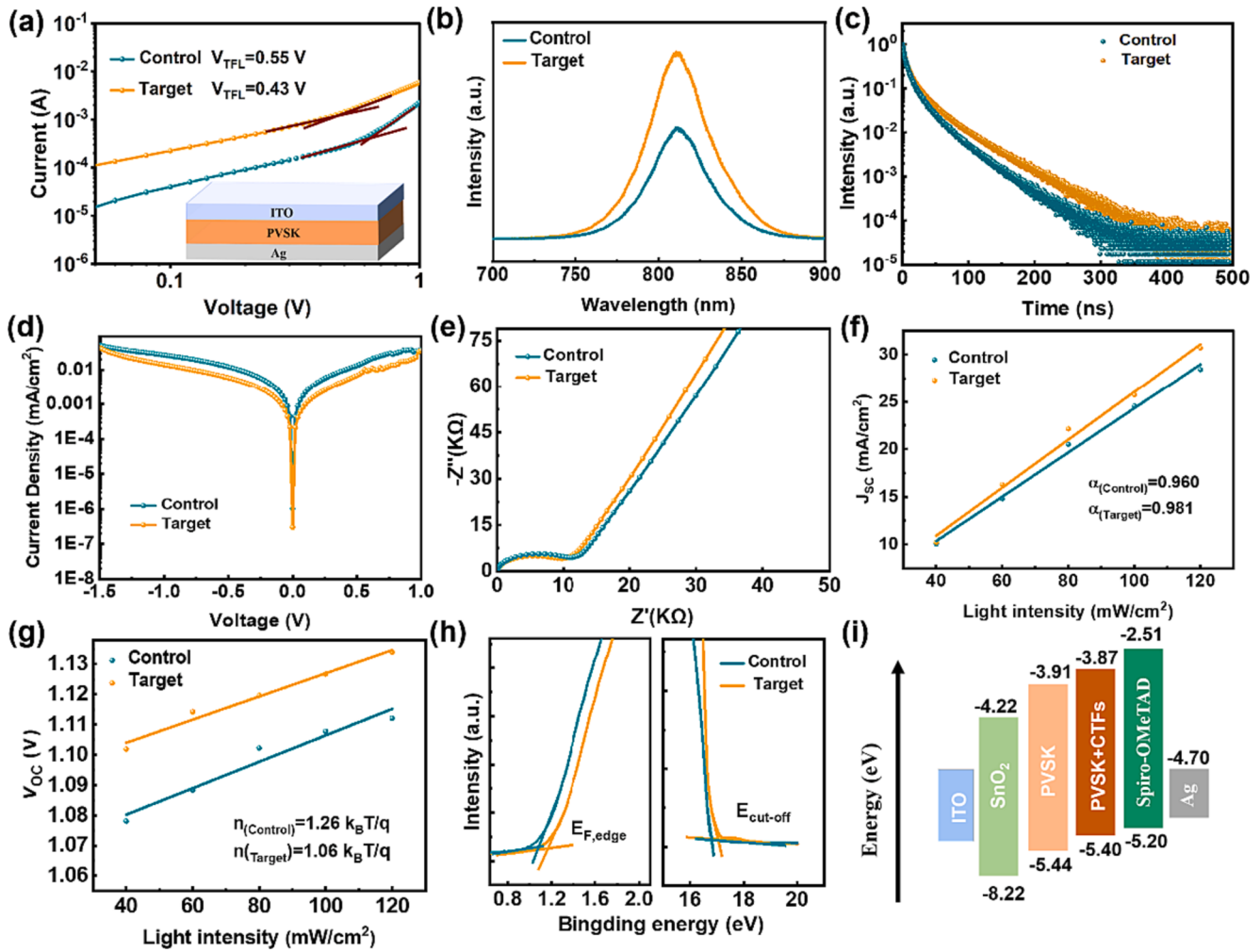


Fig. 5. (a) SCLC test based on the device with the structure of ITO/perovskite (PVSK)/Ag; (b) Steady PL and (c) TRPL spectra of perovskite films; (d) Dark J-V curves of the devices; (e) Nyquist plots of different devices measured in the dark; (f and g) J_{SC} and V_{OC} values under different light intensities for the devices; (h) UPS characterization of perovskite films; (i) Energy-level scheme for each functional layer of the device.

vacuum permittivity, V_{TFL} the trap-filled limit voltage, e the electron charge, and L the thickness of perovskite film. After introducing the CTFs, the n_t of perovskite films decreases from $4.92 \times 10^{15} \text{ cm}^{-3}$ to $3.73 \times 10^{15} \text{ cm}^{-3}$, confirming the positive effect of CTFs on passivating the perovskite defects. Steady-state photoluminescence (PL) spectra and time-resolved photoluminescence (TRPL) testing in Fig. 5b, 5c and S10 are used to further understand the recombination behavior of photo-excited carriers in perovskite films. The PL intensity of 0.20 mg/mL CTFs-modified target films is higher than that of control perovskite films, indicating that non-radiative recombination can be reduced by CTFs modification. However, the PL intensity was lower than that of the target sample when the CTFs concentration increases to 0.23 mg/mL, which is mainly due to the increased charge recombination sites due to the increased grain boundaries number. As the fitted results of TRPL spectra by the double exponential equation (2) and (3) in Fig. 5c and Table S1, the average carrier lifetime increased from 28.44 ns of control film to 42.28 ns of CTFs-modified perovskite film. The prolonged carrier lifetime can be deduced from that the CTFs material can exert strong chemical interaction with perovskite, which passivates the defects of perovskite film and reduces the defects-related non-radiative recombination loss [37].

$$I(t) = I_0 + A_1 \exp(-t/\tau_1) + A_2 \exp(-t/\tau_2) \quad (2)$$

$$\tau_{ave} = \frac{A_1 \tau_1^2 + A_2 \tau_2^2}{A_1 \tau_1 + A_2 \tau_2} \quad (3)$$

In order to study the reduced non-radiative recombination by CTFs, we conduct the dark current–voltage measurements in Fig. 5d, where a bias of 0 V is applied and the leakage current density (J_0) is related to the defect density. And the lower defect density leads to the lower J_0 [38]. The CTFs-modified device shows the reduced J_0 , revealing the reduced defect density by CTFs passivation. We further explored the charge transport and recombination behavior of devices by performing electrochemical impedance spectroscopy (EIS) measurements. As the incomplete semicircle shown in the high-frequency region, the CTFs-modified devices exhibit an increased carrier recombination resistance (R_{rec}) in Fig. 5e, because the perovskite film with reduced defects can inhibit the non-radiative recombination. In Fig. 5f-g, the dependence curves of open circuit voltage (V_{OC}) and short current density (J_{SC}) on light intensity (I) follow the following equation (5) and (6):[39]

$$V_{OC} = \frac{n k_B T \ln(I)}{q} \quad (5)$$

$$J_{SC} \propto I^\alpha \quad (6)$$

Where k_B is the Boltzmann constant, T the thermodynamic temperature, and q the electron charge. The ideal factor (n) and exponential factor (α)

can be extracted from the slope of the fitted light intensity dependent V_{OC} and J_{SC} curves. The previous study has indicated that non-radiative recombination can be ignored for n and $\alpha = 1$, but cannot be neglected when n and α deviate from 1 [40]. The n value decreases from 1.26 of control device to 1.06 of CTFs-modified device, indicating the defects induced non-radiative recombination has been significantly inhibited. Besides, the α value of CTFs-modified devices (0.981) is closer to 1 than 0.960 for control devices. The values of n and α that close to 1 indicate that CTFs can reduce non-radiative recombination. In Fig. 5h, we further studied the effect of CTFs additives on the band characteristics of perovskite films by ultraviolet photoelectron spectroscopy (UPS). Combined with the Tauc diagram in Fig. S5, the conduction band minimum (E_{CB}) and maximum of valence band (E_{VB}) of perovskite are calculated and summarized in Table S2. As the Fig. 5i shown, after modifying with CTFs, the VBM position of perovskite upward shift to ensure better energy level matching with the highest occupied molecular orbital (HOMO) energy level of Spiro-OMeTAD, which facilitates photogenerated hole extraction from perovskites to Spiro-OMeTAD [41].

Fig. 6a and Table S3 show the forward and reverse current density–voltage (J – V) curves and parameters of devices under the AM 1.5 G standard solar simulator. The performance parameters of cells prepared with different amounts of CTFs are shown in Fig. S11–S12 and Table S4. PSCs have the best photoelectric performance when CTFs concentration

is 0.20 mg/mL. The control devices show a V_{OC} of 1.09 V, a short-circuit current (J_{SC}) of 24.84 mA/cm², a fill factor (FF) of 78.52 %, and a resulting maximum PCE of 21.26 %. After introducing CTFs into the perovskite absorbing layer, all parameters, including J_{SC} , V_{OC} , and FF and PCE , are increased. The 0.20 mg/mL CTFs-modified devices exhibit a high V_{OC} of 1.12 V, a J_{SC} of 25.21 mA/cm² and a fill factor (FF) of 81.62 %, yielding a champion PCE of 23.05 %. The previous report has proved that the defects-related non-radiative recombination is one of the reasons for V_{OC} loss [42]. The V_{OC} of the target device is higher than that of the control device, mainly because CTFs can passivate the defects of the perovskite film and reduce the non-radiative recombination, which can be proved by the results of space-charge-limited-current (SCLC) curves and PL spectra. The device hysteresis is also reduced by CTFs with the reduced hysteresis factor from 0.034 to 0.024, which can be attributed to that the chemical interaction between CTFs and I^- is helpful to suppress the I^- migration. However, when the concentration increases to 0.23 mg/mL, the performance parameters of the device decrease. This is mainly because increased grain boundaries number lead to more non-radiative recombination. As a contrast, the monomer 1,4-dicyanobenzene (DCB) was also introduced into perovskite precursor solution to prepare perovskite solar cells. By comparing the revalent performance parameters in Fig. S13, it is found that the CTFs-modified device exhibits the higher PCE than monomer DCB-modified device. Encouragingly, the target device shows the higher average PCE (22.20 %

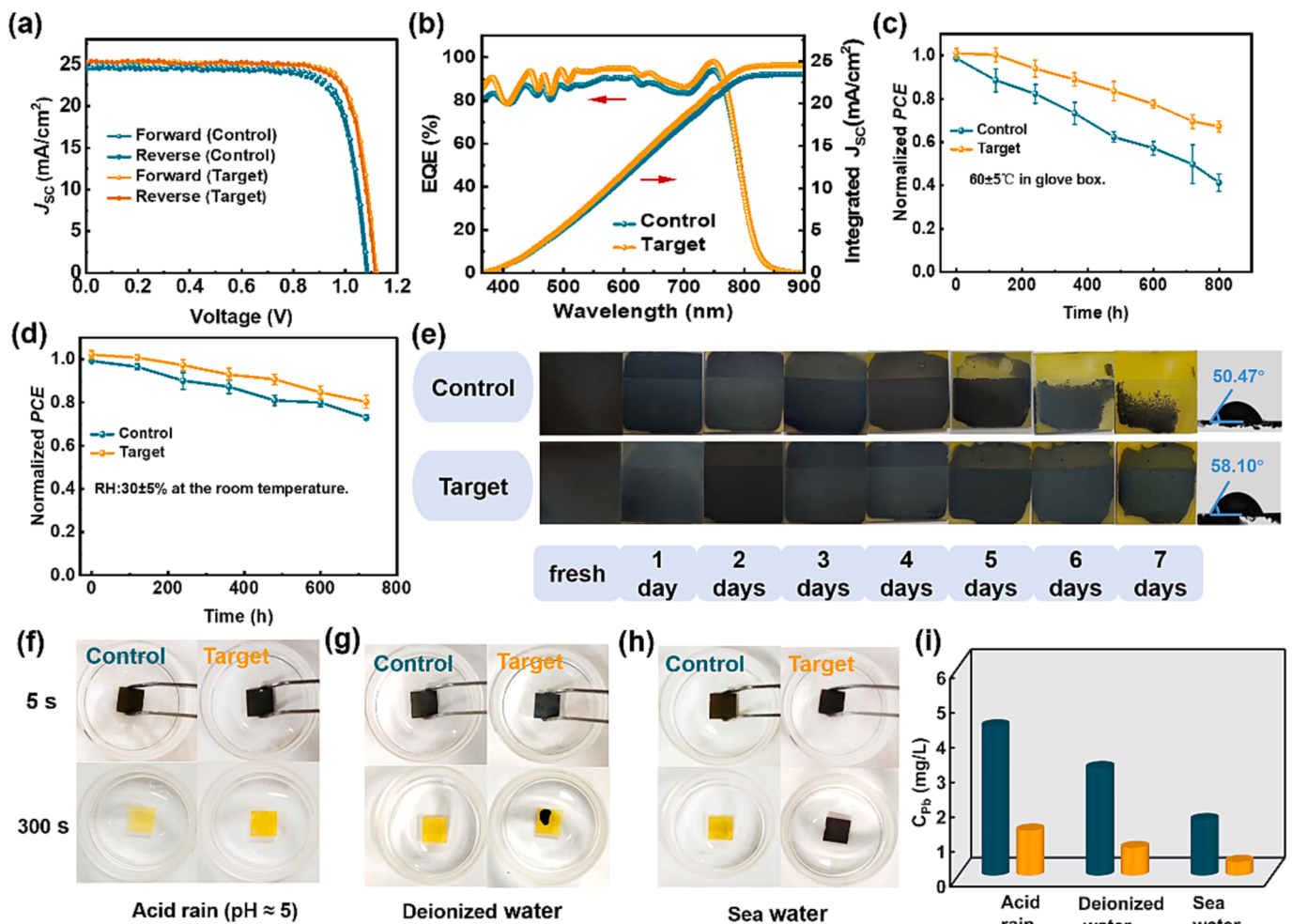


Fig. 6. (a) J – V curves of devices for control device and CTFs-modified target device; (b) EQE spectra along with integrated J_{SC} curves of the devices; Stability test of unpackaged devices aging in different conditions: (c) heating at hot plate with a temperature of $60 \pm 5^\circ\text{C}$; (d) in air with a relative humidity (RH) of $30 \pm 5\%$; (e) Evolution picture of perovskite films at room temperature with a relative humidity of $60 \pm 5\%$; Evolution diagrams of control and target perovskite films soaking in: (f) acid rain, (g) deionized water, and (h) seawater; (i) Lead concentration in the above leaching solution of perovskite films determined by inductively coupled plasma mass spectrometry (ICP-MS).

± 1.20) than that of control device ($20.66\% \pm 1.22$) in Table S5. As the Fig. S14 depicted, the target device also exhibits the high repeatability in device performances. In Fig. 6b, the target device achieves an integral photocurrent density of 24.53 mA/cm^2 , significantly higher than the 23.45 mA/cm^2 for the control devices. To investigate the effect of CTFs on stability, we have tested the stability of the control device and the target device under different environmental conditions. In Fig. S15, we have measured the steady-state current density and PCE evolution of the devices at their respective maximum power point. The control device has an output steady-state current density of 23.21 mA/cm^2 and a stable PCE of 20.19 %, whereas the CTFs-modified device produced higher output current densities and PCE (24.25 mA/cm^2 and 22.07 %). Fig. S16 shows UV – vis absorption spectra of perovskite films illuminated under simulated solar light (AM1.5G, 100 mW cm^{-2}) for 180 min. The absorption of control perovskite film decreases significantly than the target film in the range of 400–550 nm, indicating the enhanced light stability by CTFs. The inhibited I^- migration can explain the enhanced light stability. We have also investigated the thermal stability of the unpackage devices by heating them at $60 \pm 5^\circ\text{C}$ in an Ar-filled glove box in Fig. 6c and Fig. S17. After 800 h of thermal aging, the target devices can still maintain 65.59 % of the original efficiency, while the control devices can only maintain 45.38 % of the actual efficiency. We also evaluate the device stability by storing the unsealed PSCs at dark air condition with a relative humidity of 1–2 % for 1200 h (Fig. S18). The target device maintains 88.28 % of its initial efficiency, which is much superior to that of control device (77.39 %). In Fig. 6d and Fig. S19, the unencapsulated target device maintains 80.28 % of its initial PCE after storage for 720 h in air with a relative humidity of $30 \pm 5\%$, while the efficiency of the control devices decreases to 72.98 % of the initial efficiency. In Fig. S20, we tracked the light stability by illuminating the unencapsulated devices without and with CTFs modification under LED light illumination. After 100 h of continuous illumination, the CTFs-modified target device shows the better light stability, with an efficiency retention rate of 80.68 %, while the control device had an efficiency retention rate of 70.11 %. Besides, we further tracked the operational stability of these devices under continuous illumination and maximum power points. After 30 h, the efficiency of the control device quickly decays to 88.41 % of the initial efficiency, while the efficiency of the target device can still maintain 94.27 % of the initial efficiency in Fig. S21. The improved light stability of the target device is mainly attributed to the reduced non-radiative recombination and the inhibited ion migration by CTFs. In order to support the claim of the defects at grain boundary will accelerate the decomposition due to oxygen. The control and target devices are placed in an oxygen-filled atmosphere with low relative humidity (1–2 %RH) to track the stability. After 210 h, the target device can still maintain about 91.68 % of its initial efficiency, while the control device attenuates to only about 76.97 % of the initial efficiency in Fig. S22. The poor stability of control device in oxygen-filled atmosphere also explained the defects at grain boundary will accelerate the decomposition due to oxygen. In addition, we also track the stability of perovskite film at relative humidity of $60 \pm 5\%$. After seven days of aging, the control films almost degraded to yellow. On the contrast, the target perovskite film remains basically black, and only slightly degradation can be observed at the edge of the film (Fig. 6e). Fig. S23 shows the XRD patterns of aged perovskite film in air condition with the humidity of $60 \pm 5\%$ RH for seven days. It is obvious that the control film presents the higher $PbI_2/PVSK$ intensity ratio than the target film, indicating the CTFs modification can delay the degradation of perovskite under high humidity conditions (Fig. S24). After being modified by CTFs, the water contact angle increases from 50.47° to 58.10° , which can explain the increased humidity stability of target perovskite film. Above results all illustrate that the CTFs modification can enhance the device stability, which can be attributed to the passivated defects and inhibited ion migration by CTFs.

The Pb leakage of perovskite film and devices have been

quantitatively determined by ICP-MS. Firstly, lead leakage simulation of perovskite film is performed by soaking all perovskite films in the same beaker containing 20 mL of simulated solvent (deionized water, simulated acid rain, and seawater). Fig. 6h shows the leaked Pb concentration from the unencapsulated perovskite film after immersing into the simulated solution for 5 min. For the control film, the Pb concentrations leaked into the solution are 4.30 mg/L (acid rain), 3.10 mg/L (deionized water) and 1.60 mg/L (seawater), respectively. However, the simulated solutions soaked with target perovskite film exhibit the leaked Pb concentrations of 1.30 mg/L (acid rain), 0.80 mg/L (deionized water) and 0.40 mg/L (seawater), respectively. In addition, the encapsulated devices are also used for lead leak detection. We performed a drip test on damaged devices with and without CTFs to characterize lead leakage. Deionized water, simulated acid rain and simulated ocean water were dropped at the rate of 5 mL/h for 1 h, and the lead concentration was measured by ICP-MS. The experimental results show that after modification with covalent triazine, the Pb concentration of the target device decreases from 0.30 mg/L to 0.07 mg/L under deionized water, from 2.00 mg/L to 1.10 mg/L under simulated acid rain, and from 1.30 mg/L to 0.40 mg/L under simulated ocean water, respectively (Fig. S25). According to the experimental results, CTFs have the potential to reduce device's lead leakage. The significantly decreased lead leakage levels can be attributed to the strong coordination roles between CTFs and uncoordinated Pb^{2+} , which can grapple Pb^{2+} and reduce the dissociation of perovskite. On the other hand, CTFs can be used as a porous adsorbent containing abundant adsorb sites, which can prevent Pb^{2+} from leaking, thus reducing the pollution to the environment [43].

3. Conclusions

In this study, we have demonstrated an effective strategy to enhance device performances by introducing the CTFs into the perovskite films to passivate the grain boundary defects, suppress the I^- migration, and reduce Pb leakage. The nitrogen on the triazine ring contains lone pair electrons, which can passivate uncoordinated Pb^{2+} defects by generating N-Pb coordinate bond. The chemical bond interaction between N and Pb^{2+} can fix the Pb^{2+} and reduce the lead leakage content of devices. In addition, the electron-deficient nature of the triazine ring determines that it can form weak anions with electron-rich I^- based on the typical anion- π Interaction. The weak interaction between triazine ring in CTFs and I^- can immobilize I^- and inhibit its migration, thereby reducing the generation of iodine vacancies, hysteresis effect, and performance degradation caused by I^- migration. Consequently, CTFs-modified device exhibits the reduced carrier nonradiative recombination, yielding an enhanced PCE of 23.05 % and improved stability against humidity, heat and light illumination.

4. Experimental Section

4.1. Material

The ITO glass substrates were purchased from Jiangsu Yanchang Sunlaite New Energy Co., Ltd. The SnO_2 was bought from Alfa Aesar (tin (IV) oxide, 15 % in H_2O colloidal dispersion). Rubidium iodide (RbI, 99.9 %) and 1-Methyl-2-pyrrolidinone (NMP, 99.9 %) were purchased from Aladdin. Cesium iodide (CsI, 99.99 %), lead (II) iodide (PbI_2 , 99.99 %), lead (II) chloride ($PbCl_2$, 99.99 %), Lead (II) bromide ($PbBr_2$, 99.9 %), 2,2',7,7'-Tetrakis[N,N-di(4-methoxyphenyl)amino]-9,9'-spirobifluorene.

(Spiro-OMeTAD, 99.86 %), methylamine hydrochloride (MACl, 99.5 %), and formamidine hydroiodide (FAI, 99.9 %) were bought from Xi'an Polymer Light Technology Corp. Advanced Electron Technology CO. Ltd. N,N-dimethyl formamide (DMF, 99.8 %), dimethyl sulfoxide (DMSO, 99.9 %), and chlorobenzene (CB, 99.8 %) were obtained from Sigma Aldrich.

Preparation of CTFs:

The CTFs were prepared according to the previous reports. In detail, monomer 1,4-dicyanobenzene (DCB) and H₆P₄O₁₃ with a certain proportion were put into a high temperature tube and transferred to a Muffle furnace for heating at 400°C. Then the crude product obtained by the reaction is soaked in ammonia overnight and washed with ethanol, acetone and tetrahydrofuran in turn. Finally, the sample can be obtained after vacuum drying at 120°C.

4.2. Device Fabrication

The device structure in this work is ITO/SnO₂/perovskite with or without CTFs/Spiro-OMeTAD/Ag. The etched ITO glass was ultrasonically cleaned for 20 min using detergent, deionized water, and ethanol, sequentially. After being blown dry by nitrogen (99.99 %), and then the ITO was treated for 30 min with ultraviolet ozone (UV-O₃). The SnO₂ colloidal solution was prepared by combining the SnO₂ solution with deionized water at a volume ratio of 1:3. The as-prepared SnO₂ colloidal solution was filtered by the 0.22 μm polytetrafluoroethylene (PTFE) filter before use. The SnO₂ colloidal solution was spin-coated onto clean ITO glass substrates in ambient air with a spin rate of 3000 rpm for 30 s and annealed on a hot plate at 150 °C for 30 min. Afterwards, SnO₂ films were treated by UV-O₃ for 20 min. The substrate is then spin-coated with perovskite layer in an Ar gas-filled glove box. The 1.55 M perovskite precursor solution was prepared by dissolving FAI of 248.16 mg, CsI of 19.73 mg, RbI of 6.58 mg, PbI₂ of 682.73 mg, PbBr₂ of 8.53 mg, PbCl₂ of 12.74 mg, and MACl of 35 mg in the mixed solvents of DMF and DMSO (VDMF:VDMSO = 4:1). The as-prepared perovskite precursor solution was filtered by the filter before use. The 15 μL NMP solution with different content of CTFs (0.00 mg/mL, 0.17 mg/mL, 0.20 mg/mL, and 0.23 mg/mL) were introduced into perovskite precursor solution for realizing the dissolution of CTFs. During the preparation of the perovskite film, the perovskite precursor solution was rotated on the SnO₂ film at 4000 rpm for 30 s, and 80 μL of CB antisolvent was dropped at 17 s. The film was then annealed at 130 °C for 28 min. The Spiro-OMeTAD solution was prepared by mixing 72.3 mg Spiro-OMeTAD, 28.8 μL 4-tert-butyl pyridine (tBP) and 17.5 μL lithium bis(trifluoromethane) sulfonyl imide (Li-TFSI) stock solution (520 mg Li-TFSI in 1 mL acetonitrile) in 1 mL CB. The hole transport layer was then formed by spin-coating 20 μL of Spiro-OMeTAD solution onto the perovskite films at 4000 rpm for 33 s. Finally, gold counter electrode with the thickness about 100 nm was thermally evaporated on the top of Spiro-OMeTAD film under a vacuum of 3×10^{-5} Pa through using a shadow mask. For the thermal stability test, Spiro-OMeTAD/PTAA was used as the hole transport layer, which was prepared by spin-coating the mixed Spiro-OMeTAD/PTAA solution (36 mg Spiro-OMeTAD, 5 mg PTAA, 35 μL Li-TFSI (260 mg mL⁻¹ in acetonitrile) and 30 μL 4-tertbutylpyridine were dissolved in 1 mL CB) at 1500 rpm for 30 s. Except for the changes in the preparation of the hole transport layer, the preparation of other functional layers is still consistent with the above method.

4.3. Characterization

Current density–voltage (J-V) curves, the light intensity dependence curves, dark state J-V curves, the stable output current density and PCE curves were generated using a solar simulator and a Keithley 2400 source meter and the active area of the devices was defined to be 0.1 cm² by using a metal mask. The light intensity was calibrated using a light irradiation meter and a standard silicon solar cell. The J-V curves were measured from 0 V to 1.2 V (forward scan) or from 1.2 V to 0 V (reverse scan) with a scan rate of 100 mV s⁻¹. Electrochemical impedance spectroscopy (EIS) and Mott-Schottky curves were tested at the CHI760E electrochemical workstation. The stability of the unpackaged devices is tracked under five conditions: 1 %~2% RH moisture proof box, 30 ± 5 % and 60 ± 5 % RH environment, and 55°C~65°C hot table heating, an oxygen atmosphere with a relative humidity of 1 %~2% RH, and under constant light (LED source with 100 mW/cm²). An FTIR spectrometer

was used to acquire Fourier transformed infrared (FTIR) spectra (Tensor27, BRUKER, Germany). Thermo Avantage (v5.9921) software was used to analyze and interpret XPS spectra acquired from a Physical Electronics Model 5700 XPS equipment. SEM observations were carried out in ADD mode on SEM (FESEM, JEOL-JSM-6701F). The TEM measurement was carried out on a high-resolution transmission electron microscope. And the covalent triazine stripped by ball milling were ultrasonic dispersed in ethanol and used for TEM characterization.

An X-ray diffractometer (XRD) was used to characterize the crystallinity of the perovskite films (D2 PHASER Desktop XRD, BRUKER, Germany). Liquid Ultraviolet-visible (UV-vis) spectra were recorded on U-3900 UV-Visible spectrophotometer. The steady state photoluminescence (PL) curves were carried out using confocal raman systems (iHR 550 HORIBA) with laser of 532 nm. In Shanxi University's State Key Laboratory of Quantum Optics and Quantum Optics Devices, time-resolved photoluminescence (TRPL) was measured using a self-built scanning confocal system based on an inverted microscope (Nikon, TE2000-U) with a 532 nm laser. The external quantum efficiencies (EQE, Zennium CIMPS-pcs2 (Zahner)) was measured with the tunable light source (TLS03). Impedance spectroscopy measurement was performed on an electrochemical workstation (China). The PHI 5000 VersaProbe III was used to perform ultraviolet photoelectron spectroscopy (UPS) using a He I source (21.22 eV) and a negative bias of 5.0 V. The G-AFM was tested by an atomic force microscope instrument (Bruker Icon).

Lead leakage test:

Simulated seawater was prepared by mixing NaCl (26.518 mg), MgSO₄ (3.305 mg), MgCl₂ (2.447 mg), CaCl₂ (1.141 mg), KCl (0.725 mg), NaHCO₃ (0.202 mg), and NaBr (0.083 mg) into (1 mL) deionized water. Simulated acid rain was prepared by mixing H₂SO₄ (98 %) and HNO₃(68 %) with a molar ratio of 8:1 (pH≈5). The Pb concentration was detected by an ICP-MS instrument (NexION 350, PerkinElmer). The devices for lead leakage test were only encapsulated by a piece of cover glass with epoxy at the edge. Star cracks is formed on the surface of the device by ice ball impact.

4.4. Computational method

Visualize the Electrostatic potential (ESP) and Milliken charge distribution of CTFs by performing density functional theory (DFT) theoretical calculations using a Gaussian software program (B3LYP/def2TZVP). The chemical interaction between CTFs and perovskite was calculated with the Gaussian 16 software package [44] at the B3LYP level with a def2TZVP basis set [45]. The structural relaxation and static self-consistent energy calculations are performed by CP2K package at the Perdew-Burke-Ernzerhof level, DZVPMOLOPT-GTH basis sets were utilized to describe the molecules [46,47]. A FAPbI₃ perovskite slab model is constructed for the cases before and after CFTs treatment with typical (0 0 1) orientation selected on the surface, which is terminated by PbI₂. A plane-wave energy cut-off of 500 Ry has been employed. To maintain the bulk behavior of inner layers, we keep the bottom layer fixed during optimizations. The charge density difference is defined as:

$\Delta\rho = \rho_{\text{mol/sur}} - \rho_{\text{mol}} - \rho_{\text{sur}}$, where $\rho_{\text{mol/sur}}$, ρ_{mol} and ρ_{sur} are the electron density of the molecule adsorbed on surface, and the individual electron density of molecule and surface. The analyses of the DFT result were carried out by Multiwfn code [48].

CRediT authorship contribution statement

Wenjing Hou: Writing – review & editing, Supervision, Conceptualization. **Mengna Guo:** Writing – original draft, Methodology, Data curation. **Tian Sun:** Methodology. **Yaoming Xiao:** Resources. **Huan Bi:** Methodology. **Yuxi Xu:** Writing – review & editing, Resources, Methodology. **Gaoyi Han:** Writing – review & editing, Supervision, Resources.

Declaration of competing interest

The authors declare that they have no known competing financial interests or personal relationships that could have appeared to influence the work reported in this paper.

Data availability

Data will be made available on request.

Acknowledgements

This work was financially supported by the National Natural Science Foundation of China (61804091 and U21A6004), Program of State Key Laboratory of Quantum Optics and Quantum Optics Devices (No: KF201910), and Natural Science Foundation of Shanxi Province (202203021221007). And we are also grateful for the Scientific Research Start-up Funds of Shanxi University, Hundred Talents Plan of Shanxi Province, Quanzhou “Tong Jiang Scholar” Program, and Fujian Natural Science Funds for Distinguished Young Scholar (2020J06046). The author would like to acknowledge Prof. Qing Shen (The University of Electro-Communications) for the valuable discussion.

Appendix A. Supplementary data

Supplementary data to this article can be found online at <https://doi.org/10.1016/j.cej.2024.148643>.

References

- [1] Z.P. Li, Z.W. Zhang, R.M. Nie, C.Z. Li, Q.K. Sun, W. Shi, W.C. Chu, Y.T. Long, H. Li, X.M. Liu, Construction of Stable Donor-Acceptor Type Covalent Organic Frameworks as Functional Platform for Effective Perovskite Solar Cell Enhancement, *Adv. Funct. Mater.* 32 (21) (2022) 2112553.
- [2] A. Kojima, K. Teshima, Y. Shirai, T. Miyasaka, Organometal Halide Perovskites as Visible-Light Sensitizers for Photovoltaic Cells, *J. Am. Chem. Soc.* 131 (2009) 6050–6051.
- [3] <https://www.nrel.gov/pv/interactive-cell-efficiency.html>.
- [4] S.I. Rahman, B.S. Lamsal, A. Gurung, A.H. Chowdhury, K.M. Reza, B.B. Nabin Ghimire, W. Luo, R.S. Bobba, J. Pokharel, A. Baniya, A.R. Laskar, K. Emshadi, M. T. Rahman, Q. Qiao, Grain Boundary Defect Passivation of Triple Cation Mixed Halide Perovskite with Hydrazine-Based Aromatic Iodide for Efficiency Improvement, *ACS Appl. Mater. Interfaces* 12 (2020) 41312–41322.
- [5] X. Wang, Q. Zhao, Z. Li, D. Liu, C. Chen, B. Zhang, X. Sun, X. Du, L. Hao, C. Gao, Y. Li, S. Mao, Z. Shao, X. Wang, G. Cui, S. Pang, Improved Performance and Stability of Perovskite Solar Cells by Iodine-Immobilizing with Small and Flexible Bis(amide) Molecule, *Chem. Eng. J.* 451 (2023) 138559.
- [6] W. Chai, W. Zhu, J. Ma, S. Huangfu, Z. Zhang, D. Chen, J. Zhang, C. Zhang, Y. Hao, Charge-Selective-Contact-Dependent Halide Phase Segregation in CsPbIBr₂ Perovskite Solar Cells and Its Correlation to Device degradation, *Appl. Surf. Sci.* 595 (2022) 153544.
- [7] H. Zhang, K. Li, M. Sun, F. Wang, H. Wang, A.K.Y. Jen, Design of Superhydrophobic Surfaces for Stable Perovskite Solar Cells with Reducing Lead Leakage, *Adv. Energy Mater.* 11 (41) (2021) 2102281.
- [8] S. Yang, S. Chen, E. Mosconi, Y. Fang, X. Xiao, C. Wang, Y. Zhou, Z. Yu, J. Zhao, Y. Gao, F.D. Angelis, J. Huang, Stabilizing Halide Perovskite Surfaces for Solar Cell Operation with Wide-Bandgap Lead Oxyhalides, *Science* 365 (2019) 473–478.
- [9] L. Yuan, H. Luo, J. Wang, Z. Xu, J. Li, Q. Jiang, K. Yan, Quantifying the Energy Loss for a Perovskite Solar Cell Passivated with Acetamidine Halide, *J. Mater. Chem. A* 9 (8) (2021) 4781.
- [10] T. Li, Y. Pan, Z. Wang, Y. Xia, Y. Chen, W. Huang, Additive Engineering for Highly Efficient Organic-Inorganic Halide Perovskite Solar Cells: Recent Advances and Perspectives, *J. Mater. Chem. A* 5 (25) (2017) 12602.
- [11] F. Zhang, K. Zhu, Additive Engineering for Efficient and Stable Perovskite Solar Cells, *Adv. Energy Mater.* 10 (13) (2019) 1902579.
- [12] X. Ma, L. Yang, X. Shang, M. Li, D. Gao, C. Wu, S. Zheng, B. Zhang, J. Chen, C. Chen, H. Song, Grain Boundary Defect Passivation by in situ Formed Wide-Bandgap Lead Sulfate for Efficient and Stable Perovskite Solar Cells, *Chem. Eng. J.* 426 (2021) 130685.
- [13] Y. Lao, S. Yang, W. Yu, H. Guo, Y. Zou, Z. Chen, L. Xiao, Multifunctional pi-Conjugated Additives for Halide Perovskite, *Adv. Sci.* 9 (17) (2022) 2105307.
- [14] S. Liu, Y. Guan, Y. Sheng, Y. Hu, Y. Rong, A. Mei, H. Han, A Review on Additives for Halide Perovskite Solar Cells, *Adv. Energy Mater.* 10 (13) (2019) 1902492.
- [15] J. Zhang, J. Duan, Q. Guo, Q. Zhang, Y. Zhao, H. Huang, Y. Duan, Q. Tang, A Universal Grain “Cage” to Suppress Halide Segregation of Mixed-Halide Inorganic Perovskite Solar Cells, *ACS Energy Lett.* 7 (10) (2022) 3467–3475.
- [16] Z. Li, Z. Zhang, R. Nie, C. Li, Q. Sun, W. Shi, W. Chu, Y. Long, H. Li, X. Liu, Construction of Stable Donor-Acceptor Type Covalent Organic Frameworks as Functional Platform for Effective Perovskite Solar Cell Enhancement, *Adv. Funct. Mater.* 32 (2022) 2112553.
- [17] R. Nie, W. Chu, Z. Li, H. Li, S. Chen, Y. Chen, Z. Zhang, X. Liu, W. Guo, S. Seok, Simultaneously Suppressing Charge Recombination and Decomposition of Perovskite Solar Cells by Conjugated Covalent Organic Frameworks, *Adv. Energy Mater.* 12 (33) (2022) 2200480.
- [18] X. Zhou, L. Qiu, R. Fan, J. Zhang, S. Hao, Y. Yang, Heterojunction Incorporating Perovskite and Microporous Metal-Organic Framework Nanocrystals for Efficient and Stable Solar Cells, *Nanomicro Lett.* 12 (1) (2020) 80.
- [19] S. Wu, Z. Li, M.Q. Li, Y. Diao, F. Lin, T. Liu, J. Zhang, P. Tieu, W. Gao, F. Qi, X. Pan, Z. Xu, Z. Zhu, A.K. Jen, 2D Metal-Organic Framework for Stable Perovskite Solar Cells with Minimized Lead Leakage, *Nat. Nanotechnol.* 15 (11) (2020) 934–940.
- [20] T. Sun, Y. Liang, W. Luo, L. Zhang, X. Cao, Y. Xu, A General Strategy for Kilogram-Scale Preparation of Highly Crystal-line Covalent Triazine Frameworks, *Angew. Chem. Int. Ed.* 61 (25) (2022) e202203327.
- [21] T. Sun, Y. Liang, Y. Xu, Rapid, Ordered Polymerization of Crystalline Semiconducting Covalent Triazine Frameworks, *Angew. Chem. Int. Ed.* 61 (4) (2022) e202113926.
- [22] D.X. Wang, Q.Q. Wang, Y. Han, Y. Wang, Z.T. Huang, M.X. Wang, Versatile Anion-pi Interactions Between Halides and a Conformationally Rigid Bis(Tetraoxacalix[2]Arene [2]Triazine) Cage and Their Directing Effect on Molecular Assembly, *Chem. Eur. J.* 16 (44) (2010) 13053–13057.
- [23] A.P. Côté, A.I. Benin, N.W. Ockwig, M. O’Keeffe, A.J. Matzger, O.M. Yaghi, Porous, Crystalline, Covalent Organic Frameworks, *Science* 310 (5751) (2005) 1166–1170.
- [24] Q. He, Y.F. Ao, Z.T. Huang, D.X. Wang, Self-Assembly and Disassembly of Vesicles as Controlled by Anion-pi Interactions, *Angew. Chem. Int. Ed.* 54 (40) (2015) 11785–11790.
- [25] D.X. Wang, Q.Y. Zheng, Q.Q. Wang, M.X. Wang, Halide Recognition by Tetraoxacalix[2]Arene [2]Triazine Receptors: Concurrent Noncovalent Halide-pi and Lone-pair-pi Interactions in Host-Halide-Water Ternary Complexes, *Angew. Chem. Int. Ed.* 47 (39) (2008) 7485–7488.
- [26] D.X. Wang, M.X. Wang, Anion-pi Interactions: Generality, Binding Strength, and Structure, *J Am Chem Soc.* 135 (2) (2013) 892–897.
- [27] X. Zuo, B. Kim, B.B. Liu, D.M. He, L. Bai, W.Q. Wang, C.Y. Xu, Q.L. Song, C.Y. Jia, Z.G. Zang, D. Lee, X. Li, J.Z. Chen, Passivating Buried Interface via Self-Assembled Novel Sulfonium Salt Toward Stable and Efficient Perovskite Solar Cells, *Chem. Eng. J.* 431 (2022) 133209.
- [28] L. Zhao, S.R. Sun, J.X. Lin, L. Zhong, L.H. Chen, J. Guo, J. Yin, H.N. Alshareef, X. Q. Qiu, W.L. Zhang, Defect Engineering of Disordered Carbon Anodes with Ultra-High Heteroatom Doping Through a Supermolecule-Mediated Strategy for Potassium-Ion Hybrid Capacitors, *Nanomicro Lett.* 15 (3) (2023) 41.
- [29] T. Lu, Q. Chen, Independent gradient model based on Hirshfeld partition: A New Method for Visual Study of Interactions in Chemical Systems, *J Comput Chem.* 43 (8) (2022) 539–555.
- [30] Y.-H. Lin, N. Sakai, P. Da, J. Wu, H.C. Sansom, A.J. Ramadan, S. Mahesh, J. Liu, R. D.J. Oliver, J. Lim, L. Aspitarte, K. Sharma, P.K. Madhu, A.B. Morales-Vilches, P. K. Nayak, S. Bai, F. Gao, C.R.M. Grovenor, M.B. Johnston, J.G. Labram, J. R. Durrant, J.M. Ball, B. Wenger, B. Stannowski, H.J. Snaith, A Piperidinium Salt Stabilizes Efficient Metal-Halide Perovskite Solar Cells, *Science* 369 (2020) 96–102.
- [31] S. Chen, X. Dai, S. Xu, H. Jiao, L. Zhao, J. Huang, Stabilizing Perovskite-Substrate Interfaces for High-Performance Perovskite Modules, *Science* 373 (2021) 902–907.
- [32] S. Chen, X. Xiao, H. Gu, J. Huang, Iodine Reduction for Reproducible and High-Performance Perovskite Solar Cells and Modules, *Sci. Adv.* 7 (2021) eabe8130.
- [33] S. Wang, Y. Jiang, E.J. Juarez-Perez, L.K. Ono, Y. Qi, Accelerated Degradation of Methylammonium Lead Iodide Perovskites Induced by Exposure to Iodine Vapour, *Nat. Energy* 2 (2016) 16195.
- [34] W. Fan, S. Zhang, C. Xu, H. Si, Z. Xiong, Y. Zhao, K. Ma, Z. Zhang, Q. Liao, Z. Kang, Y. Zhang, Grain Boundary Perfection Enabled by Pyridinic Nitrogen Doped Graphdiyne in Hybrid Perovskite, *Adv. Funct. Mater.* 31 (34) (2021) 2104633.
- [35] R. Fan, Q. Song, Z. Huang, Y. Ma, M. Xiao, X. Huang, H. Zai, J. Kang, H. Xie, Y. Gao, L. Wang, Y. Zhang, L. Wang, F. Wang, X. Zhang, W. Zhou, N. Li, X. Wang, Y. Bai, G. Liu, Q. Chen, L. Wang, H. Zhou, Tungstate-mediated In-situ Passivation of Grain Boundary Grooves in Perovskite Solar Cells, *Angew. Chem. Int. Ed.* 62 (24) (2023) e202303176.
- [36] C. Liu, H. Su, Y. Pu, M. Guo, P. Zhai, L. Liu, H. Fu, 3D Polydentate Complexing Agents for Passivating Defects and Modulating Crystallinity for High-Performance Perovskite Solar Cells, *Adv. Funct. Mater.* 33 (17) (2023) 2212577.
- [37] X. Yuan, R. Li, Z. Xiong, P. Li, G.O. Odunmbaku, K. Sun, Y. Deng, S. Chen, Synergistic Crystallization Modulation and Defects passivation via Additive Engineering Stabilize Perovskite Films for Efficient Solar Cells, *Adv. Funct. Mater.* 33 (24) (2023) 2215096.
- [38] W. Wu, X. Dong, G. Liu, X. Pan, H. Zheng, Regulating Coordination by Multi-Configurational Alkaloid-Based Passivation Molecules for High-Performance Perovskite Photovoltaics, *Chem. Eng. J.* 452 (2023) 139535.
- [39] Y. Zhang, C. Sun, B. Huang, H. Yu, Reduced Open-Circuit Voltage Loss of Perovskite Solar Cells via Forming pi/pi+ Homojunction and Interface Electric Field on the Surfaces of Perovskite Film, *Adv. Energy Mater.* 12 (47) (2022) 2202542.
- [40] B. Liu, R. Li, Q. Zhuang, X. Yu, S. Gong, D. He, Q. Zhou, H. Yang, X. Chen, S. Lu, Z.-X. Xu, Z. Zang, J. Chen, Bottom-up Holistic Carrier Management Strategy Induced Synergistically by Multiple Chemical Bonds to Minimize Energy Losses for Efficient and Stable Perovskite Solar Cells, *J. Energy Chem.* 76 (2023) 277–287.

- [41] Y. Kong, W. Shen, H. Cai, W. Dong, C. Bai, J. Zhao, F. Huang, Y.B. Cheng, J. Zhong, Multifunctional Organic Potassium Salt Additives as the Efficient Defect Passivator for High-Efficiency and Stable Perovskite Solar Cells, *Adv. Funct. Mater.* 33 (25) (2023) 2300932.
- [42] W. Zhang, H. Liu, X. Qi, Y. Yu, Y. Zhou, Y. Xia, J. Cui, Y. Shi, R. Chen, Hsing-Lin Wang, Oxalate Pushes Efficiency of CsPb_{0.7}Sn_{0.3}Br₂ Based All-Inorganic Perovskite Solar Cells to over 14%, *Adv. Sci.* 9 (2022) 2106054.
- [43] E. Saputra, B.A. Prawiranegara, H. Sugesti, M.W. Nugraha, P.S. Utama, Covalent Triazine Framework: Water Treatment Application, *J. Water Process. Eng.* 48 (2022) 102874.
- [44] M. J. Frisch, G. W. Trucks, H. B. Schlegel, G. E. Scuseria, M. A. Robb, J. R. Cheeseman, G. Scalmani, V. Barone, G. A. Petersson, H. Nakatsuji, X. Li, M. Caricato, A. V. Marenich, J. Bloino, B. G. Janesko, R. Gomperts, B. Mennucci, H. P. Hratchian, J. V. Ortiz, A. F. Izmaylov, J. L. Sonnenberg, Williams, F. Ding, F. Lipparini, F. Egidi, J. Goings, B. Peng, A. Petrone, T. Henderson, D. Ranasinghe, V. G. Zakrzewski, J. Gao, N. Rega, G. Zheng, W. Liang, M. Hada, M. Ehara, K. Toyota, R. Fukuda, J. Hasegawa, M. Ishida, T. Nakajima, Y. Honda, O. Kitao, H. Nakai, T. Vreven, K. Throssell, J. A. Montgomery Jr., J. E. Peralta, F. Ogliaro, M. J. Bearpark, J. J. Heyd, E. N. Brothers, K. N. Kudin, V. N. Staroverov, T. A. Keith, R. Kobayashi, J. Normand, K. Raghavachari, A. P. Rendell, J. C. Burant, S. S. Iyengar, J. Tomasi, M. Cossi, J. M. Millam, M. Klene, C. Adamo, R. Cammi, J. W. Ochterski, R. L. Martin, K. Morokuma, O. Farkas, J. B. Foresman, D. J. Fox, Wallingford, CT, 2016.
- [45] A.D. Becke, Density-functional thermochemistry. III. The Role of Exact Exchange, *J. Chem. Phys.* 98 (1993) 5648–5652.
- [46] J. Hutter, M. Iannuzzi, F. Schiffmann, J. VandeVondele, cp2k: Atomistic Simulations of Condensed Matter Systems, *Wires Comput Mol Sci* 4 (2014) 15–25.
- [47] J.P. Perdew, K. Burke, M. Ernzerhof, Generalized Gradient Approximation Made Simple, *Phys Rev Lett* 77 (1996) 3865.
- [48] T. Lu, F. Chen, Multiwfns: A Multifunctional Wavefunction Analyzer, *J. Comput. Chem.* 33 (2012) 580–592.